Article

Implementing an Analytical Model to Elucidate the Impacts of Nanostructure Size and Topology of Morphologically Diverse Zinc Oxide on Gas Sensing

Sanju Gupta [1,2,3,*] and Haiyang Zou [4,5]

1 Faculty of Electronics, Telecommunication and Informatics, Department of Metrology and Optoelectronics, Gdansk University of Technology, Narutowicza Str. 11/12, 80-233 Gdansk, Poland
2 Advanced Materials Center, Gdansk University of Technology, 80-233 Gdansk, Poland
3 Department of Physics, Pennsylvania State University, University Park, PA 16802, USA
4 College of Materials Science and Engineering, Sichuan University, Chengdu 610065, China; zhy@scu.edu.cn
5 School of Materials Science and Engineering, Georgia Institute of Technology, Atlanta, GA 30332, USA
* Correspondence: sgup77@gmail.com

Abstract: The development of state-of-the-art gas sensors based on metal oxide semiconductors (MOS) to monitor hazardous and greenhouse gas (e.g., methane, CH_4, and carbon dioxide, CO_2) has been significantly advanced. Moreover, the morphological and topographical structures of MOSs have significantly influenced the gas sensors by means of surface catalytic activities. This work examines the impact of morphological and topological networked assembly of zinc oxide (ZnO) nanostructures, including microparticles and nanoparticles (0D), nanowires and nanorods (1D), nanodisks (2D), and hierarchical networks of tetrapods (3D). Gas sensors consisting of vertically aligned ZnO nanorods (ZnO–NR) and topologically interconnected tetrapods (T–ZnO) of varying diameter and arm thickness synthesized using aqueous phase deposition and flame transport method on interdigitated Pt electrodes are evaluated for methane detection. Smaller-diameter nanorods and tetrapod arms (nanowire-like), having higher surface-to-volume ratios with reasonable porosity, exhibit improved sensing behavior. Interestingly, when the nanorods' diameter and interconnected tetrapod arm thickness were comparable to the width of the depletion layer, a significant increase in sensitivity (from 2 to 30) and reduction in response/recovery time (from 58 s to 5.9 s) resulted, ascribed to rapid desorption of analyte species. Additionally, nanoparticles surface-catalyzed with Pd (~50 nm) accelerated gas sensing and lowered operating temperature (from 200 °C to 50 °C) when combined with UV photoactivation. We modeled the experimental findings using a modified general formula for ZnO methane sensors derived from the catalytic chemical reaction between methane molecules and oxygen ions and considered the structural surface-to-volume ratios (S/V) and electronic depletion region width (L_d) applicable to other gas sensors (e.g., SnO_2, TiO_2, MoO_3, and WO_3). Finally, the effects of UV light excitation reducing detection temperature help to break through the bottleneck of ZnO-based materials as energy-saving chemiresistors and promote applications relevant to environmental and industrial harmful gas detection.

Keywords: nanostructured ZnO; gas sensing; surface-catalyzed; selectivity; analytical modeling

1. Introduction

The development of various gas sensors to monitor toxic, hazardous, and greenhouse gas emissions (GHG), including carbon dioxide (CO_2), as well as carbon monoxide (CO),

has been intensive [1–3]. Methane (CH_4) is an equally potent GHG that has more than eighty times the warming power of CO_2 over the first 20 years after it reaches the Earth's atmosphere. Even though CO_2 and CO have a longer-lasting effect, CH_4 sets the pace for warming in the short term. Cutting methane gas emissions to slow down global warming as we decarbonize energy systems is critical. About 30% of today's global warming driven by methane emissions is from agricultural livestock, in general, and specifically from ruminant animals, which produce CH_4 as a byproduct of digestion and microbial fermentation [4–6]. Toxic gases released routinely in environments other than CH_4 (CO, NH_3, etc.), as well as volatile organic compounds (VOCs), are degrading to humans and animals alike. The alarming rise in environmental health and safety issues caused by rapid urbanization, industrialization, vehicle exhaust gases, and agricultural sectors has led to modernizing chemical sensing technologies to continuously monitor the atmosphere, enabled by engineered materials, to combat the quality-of-life issues and deleterious work environment [7]. Accordingly, various health agencies recommend short-time exposure limits for both toxic gases and VOC. Therefore, the performance of reliable gas sensors such as an "electronic nose" must be improved, with key attributes of high sensitivity (limit of detection, LOD), response magnitude, selectivity, faster response/recovery times, and stability [8,9], with an optimal operating temperature (energy-saving), not just by tailoring the morphology and structure of sensing materials, but also by supplementing the experimental design with analytical modeling. Figure 1a provides a gas concentration sensing range depending on the sensor type and corresponding morphological dimensions [10,11]. Among many gas sensing materials, metal oxide semiconductors (MOSs) exhibit a superior performance over other sensors due to their excellent physical and chemical properties and unique structure. These materials have a reasonable wide band gap, allowing them to have a full spectrum of electronic properties (insulating $\rightleftharpoons$ semiconducting) [10,11]. Additionally, the properties of MOSs are often greatly affected by the material size at the nanoscale, showing unique properties due to the nano effect. For example, the electrical properties undergo significant changes, creating a good gas sensing material. Thus, nanostructured MOS gas sensors have enormous potential in achieving the required performance, attributed to their versatility arising from the diverse morphological surfaces, hierarchical topologies, rich catalytic surface chemistry related to interconnected grains, higher surface area (higher porosity), large surface-to-volume (S/V) ratio, shorter diffusion lengths, and ease of fabrication using low-cost manufacturing (screen printing), along with their ability to detect multiple gases desirably and discernably [12,13]. The ubiquitous porosity of MOSs enhances gas diffusion through improved accessibility to nanograins and nanocrystallites and increased catalytically active sites, resulting in enhanced performance [14–19].

Among the numerous inorganic MOS materials explored, zinc oxide (ZnO) has had much attention in microscale devices for gas sensing, in addition to optical emitters, piezoelectric transduction and actuation, two-dimensional electron gases, and neuromorphic computing from extended and oriented nanostructures. ZnO is a II–VI semiconductor with a wurtzite crystal structure possessing 13 fast growth directions, [0001], <0110>, and <2110>; 12 lower-energy facets, {01$\bar{1}$0} and {2$\bar{1}\bar{1}$0}; and a pair of polar surfaces, {0001}, facilitating the formation of unique micro/nanostructure ensembles with functional morphological versatility (see Figure 1b) [20,21]. Moreover, ZnO has a wide electronic bandgap of 3.37 eV, and it is an *n*-type semiconductor due to having abundant point defects (oxygen vacancies, Vo) and interstitial Zn (I_{Zn}) [22,23], useful for a range of optoelectronic devices [24], namely photocatalytic energy conversion [25], physical (UV) and chemical detection sensors at a molecular level [26,27], decomposition of VOC [28], single-photon emitters for quantum information science, secure communications [29,30], and UV astronomy. The diverse morphologies of ZnO include zero-dimensional (0D) quantum dots,

microparticles, nanoparticles [31], one-dimensional (1D) nanowires, nanofibers, nanorods, two-dimensional (2D) nanosprings, nanodisks, nanosheets, nanoribbons, nanowhiskers, three-dimensional (3D) hierarchical nanobrushes, and tetrapod assemblies, as illustrated in Figure 1b. The advancement of facile, cost-effective, and direct fabrication methods has promoted a significant boom in complex nanostructures with controlled morphology, orientation, and appealing physical (optical, electronic, and mechanical) and chemical (photo/catalytical) properties for designing reproducible gas sensors [32]. Nevertheless, diverse and controlled ZnO hierarchical structures (nanoflowers, nanocages, tetrapods, etc.) have been synthesized through ambient solvothermal, hydrothermal, sol-gel, flame transport, low-temperature aqueous phase, and chemical bath deposition methods [33–39]. Vast literature reports, including this work, have claimed that the aggregate morphology, size/dimension, role of exposed polar facets, and topology of ZnO nanostructures have a strong impact on sensing performance (response magnitude, sensitivity, and selectivity) characteristics [40–42]. For instance, Yamazoe et. al. [43] found an inverse correlation between the response and its grain size, which may influence the width of the space-charge region and Schottky contacts while aiding the chemisorption of gas molecules and the sensing process. Later, Seiyama et. al., reported the performance of ZnO films with good response magnitude and enhanced sensitivity by the addition of noble metals (Pt and Pd) [44,45]. Yamazoe et. al. [45] also proposed a chemical sensitization mechanism to improve gas sensing, where surface functionalization with metal nanoparticles (e.g., $Pt-SnO_2$ and $Pd-SnO_2$) facilitated the chemical reaction between the target gas and the MOS surface through the spill-over phenomenon [17,46–49]. Fundamentally, different conceptual and analytical models have been employed to describe sensing mechanistic pathways, and it is still a subject of intense research discussion. The proposed contact-controlled [5,50–53] and surface-depletion [15,54] models are widely accepted to explain the enhanced gas sensing properties of ZnO nanostructures. Chen et. al. [55] and Gupta et. al. [17,46] have used the space-charge region (SCR) model to explain the ultrasensitive ethanol and methane gas sensing performance of ZnO nanoflowers or nanowhiskers consisting of 15–20 nm thick nanowires, 100 nm thick nanorods, and 50 nm nanoneedle arms of tetrapods, respectively. Additionally, density functional theory (DFT) calculations and molecular dynamics (MD) were also employed to understand the sensing mechanism of ZnO nanostructures by gaining insights into the interaction between surface species with the target gas molecules and their orientation [56–59]. Moreover, while most of the articles discuss sensor characteristics operating at higher temperatures (200–350 °C), limiting their practical applicability, few reports have attempted to reduce the operating temperature in combination with photoactivation alongside thermal activation and *pn* junction devices operating in reverse bias, enabling depletion-assisted enhanced sensitivity [17,46]. Despite these significant efforts, a deeper understanding is still needed to design efficient chemical gas sensors that can operate at reduced or room temperature [39–41].

The main accent of this work is to examine the controlled morphology-promoted methane gas sensor response complemented with an analytical model to gain further insights into the mechanism. Briefly, the ZnO-based sensors possess a response magnitude (sensitivity) of exponential form, presented empirically as (RM) $S_g = a\, C\, g(b)$, where C_g is the target gas partial pressure in direct proportion to its concentration, and the response magnitude is characterized by pre-factor a and exponent b parameters. The b value is usually equal to 1 or rational (=0.5), depending upon the charge of surface oxygen species. Based on such empirical formulation, Hongsith and coworkers attempted to generalize the formula for ZnO-based sensors implemented in this study [60,61]. However, there is still no general model or analytical formula to explain all circumstances or factors influencing methane sensors based on nanoscale ZnO structures. Thus, it is interesting to utilize

the existing simplified model considering morphology, size, dimension, and electronic properties to describe the response characteristics of ZnO sensors developed here in this work. We focused on two different morphologies, including aggregated, vertical-standing 1D nanorod (ZnO–NR) arrays synthesized using liquid-phase deposition on seeded p–Si (100) substrates and a 3D tetrapod (T–ZnO) network with interconnected arms fabricated using flame transport synthesis as thin film sensors on prefabricated Pt IDE that are also surface-catalyzed with Pd nanoparticles (~40–60 nm) [Pd_{cat}/ZnO–NR and Pd_{cat}/T–ZnO] [17,46,62]. In addition to achieving a good response from these sensors, they showed faster recovery characteristics, a lower limit of detection, and good moisture tolerance. The response formula helped to explain signal enhancement controlled by nanorod diameter, tetrapod arm thickness, and interconnectedness, thereby determining the level of porosity enhancing the surface-to-volume ratio and decreased surface depletion layer.

Figure 1. Gas sensor development based on various ZnO morphologies. (**a**) Gas concentration sensing ranges depending upon the type of gas sensor. (**b**) Preferential growth direction of hexagonal ZnO wurtzite crystal shown with crystal facets and structures in dimensions from 3D to 0D typically grown along [0001] direction. Also shown are examples, diameter (D), and thickness (L) of nanostructures.

2. Materials and Methods

The detailed preparation of ZnO nanorods and tetrapod sensors as chemiresistors on interdigitated Pt electrodes (Pt IDE) deposited via a dry etch process is reported elsewhere (see Figure 2A schematic) [17,46,62]. Zinc oxide nanorod (ZnO–NR) assembly was synthesized using an aqueous phase deposition method on seeded p–Si (100) substrates. Briefly, a 25 mM zinc acetate in ethanol seed solution was prepared with 40 wt.% Au nanoparticles and spin-coated, followed by annealing at 350 °C for 30 min, to prepare an effective seed layer. The ZnO–NR growth solution was prepared by mixing equal volumes of 50 mM hexamethylenetetramine (HMTA) and 50 mM zinc nitrate solutions, which were stirred for 15 min before growth. The seeded substrates were placed vertically in sealed contain-

ers containing 25 mL growth solution in a box furnace at 86 °C for 8 h. After removing from the furnace, they were washed with isopropyl alcohol (IPA), rinsed with deionized (DI) water, and dried. As for tetrapod ZnO (T–ZnO) assembly, it was carried out via the direct flame transport synthesis (FTS) method utilizing zinc nanoparticles with an average particle size of 40–60 nm and polyvinyl butyral (PVB) precursors [5,46]. The solution was drop-casted onto cleaned p–Si (001) substrates (1×1.5 cm^2) with Pt IDE. The samples were dried at 60 °C for 8 h to evaporate the excess solution. The diameter of the nanorods varied between 50 nm, 150 nm, and 300 nm by deposition time (4–12 h), and tetrapod arm thickness ranged between 50 nm, 300 nm, and 500 nm, controlled by thermal treatment in a box furnace (~1100 °C for 4–8 h). The catalytic Pd nanoparticles were synthesized from a solution containing palladium chloride (PdCl$_2$) and polyvinylpyrrolidone (PVP) in methanol with a molar ratio of 0.25 mM Pd: 0.01 mM PVP. A small quantity of the solution (40–60 μL) was used to coat the sample area onto the ZnO–NR (Pd$_{cat}$/ZnO–NR) and T–ZnO (Pd$_{cat}$/T–ZnO) films, cured under UV A light (λ = 365 nm), and annealed at 400 °C for 30 min for the removal of polymeric residue and Pd nanoparticle crystallization. All the chemicals were purchased from Sigma–Aldrich (St. Louis, MO, USA), and they were used without further purification.

The samples were characterized using field emission scanning electron microscopy (FESEM, Model Apreo S, Thermo Scientific, Waltham, MA, USA) to reveal the surface morphology. XRD was performed with a CuKα radiation source (λ = 1.5405 Å) in the 2θ range of 20–60° operating at 40 kV and 40 mA. Photoluminescence (PL) spectroscopy (Edinburgh Instruments FLS1000, Livingston, UK) was utilized to investigate the optical properties at room temperature. The ZnO–NR and T–ZnO films were evaluated for CH$_4$ gas sensing performance as a function of methane concentration mixed with synthetic dry air with contacts fabricated on Pt IDE electrodes in a custom-made sensing chamber attached to a Keithley 2401 electrometer and KickStart Instrument Control software ver. 2.11.2 (Keithley, A Tektronix Company, Cleveland, OH, USA) to measure the current-voltage-temperature (I-V-T) response with a constant voltage of 10 V during sensing operation (see refs. [17,46] for details and schematic of the experimental test system). Briefly, it consisted of a cylindrical stainless steel vacuum chamber with an inlet and outlet for gases placed horizontally and coaxially inside a power supply, which was calibrated (5.4 °C/V for SiO$_2$/Si substrates) for a resistively heated ceramic heater with a 5×5 cm^2 constant temperature zone, as well as the sensor response in the dark and under UV A illumination in the gas sensing chamber. Industrial grade dry synthetic air (20% O$_2$ and 80% N$_2$) was used as the carrier gas for ultrapure methane (Air Products, Allentown, PA, USA), which was mixed in proportion. Each gas cylinder was connected to a mass flow controller (MFC) (Omega Engineering Inc., Norwalk, CT, USA) to control the gas flow and mixing ratio of the two gases, and the resulting concentration of methane into the chamber was precisely controlled. The estimated flow of the analyte in the ambient atmosphere varied from 100 ppm (0.01%) to 10,000 ppm (1%), with a relative humidity of 20–22%, the latter of which is too low to affect the sensing response. Also, during the testing, the gas pressure of the sensor was approximately 0.5 atm. Each experiment was repeated at least three times or with at least three samples of the same dimension, and the maximum variation from the optimized result of about ±5% was recorded, indicating 95% reproducibility. The response magnitude (RM), limit of detection/sensitivity, and response and recovery times of the films were determined from resistance measurements with the target gas mixed with synthetic air. The response magnitude was calculated using $RM = Ra/Rg$, where Ra resistance in air, R_g resistance in methane, and the response percentage/percentile can also be determined as follows: $R\,(\%) = (R_a - R_g)/R_g \times 100$. As for the sensitivity, it is typically derived from the slope of the calibration curve, that is, sensor response versus target gas concentration, C_g.
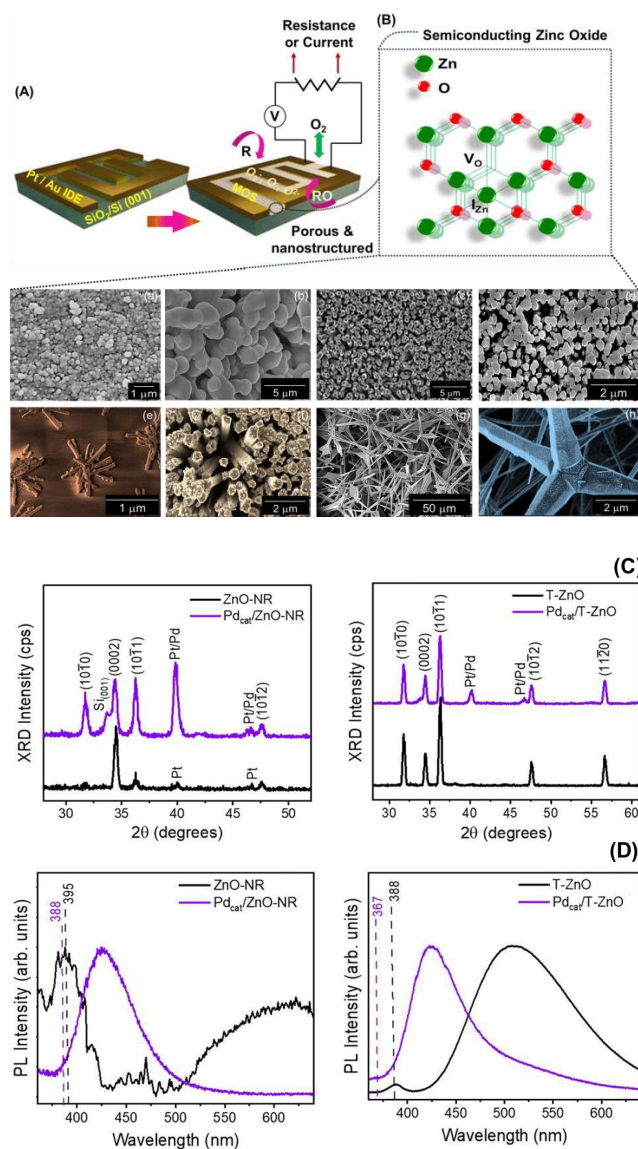
Figure 2. Surface morphology of various nanoscale ZnO, crystal structure, and optical properties. (**A**) Schematic of semiconducting metal oxide (MOS) gas sensor as chemiresistor along with ZnO crystal structure with oxygen vacancy (V_O) and interstitial Zn (I_{Zn}) point defects. (**B**) FESEM images of ZnO structures: (**a**) Nanoparticles, NP; (**b**) Microparticles, MP; (**c**) Nanowires; (**d**) Nanorods (ZnO–NR); (**e**,**f**) Pdcat/ZnO–NR; (**g**) hierarchical tetrapods (T–ZnO); and (**h**) Pdcat/T–ZnO, thin film assembly. (**C**) (Top panels) X-ray diffractograms of ZnO–NR, Pdcat/ZnO–NR, T–ZnO, Pdcat/T–ZnO, showing characteristic peaks of ZnO. (**D**) (Bottom panels) Room temperature photoluminescence (PL) spectra of ZnO–NR, Pdcat/ZnO–NR, T–ZnO, and Pdcat/T–ZnO, showing light emission peaks related to surface oxygen vacancies and other intrinsic defects.

3. Results and Discussion

3.1. Structural, Optical, and Electrical Properties

Both ZnO nanorods and tetrapods have significantly different morphologies and structures with exposed facets, which allow them to have distinctive chemical and physical properties (see Figure 2). The nanorod is a 1D structure with nonpolar exposed facets, and tetrapods are a complex network of arms interconnected to a core forming 3D morphology exposing polar facets and a curved surface, as seen in the FE-SEM images in Figure 2B(a)–(h), as well as ZnO microparticles, nanoparticles, nanowires, and Pd-catalyzed sensor materials revealing surface morphology. The ZnO–NR had well-defined hexagonal-shaped rods of 150 nm diameter [17]. The tetrapod ZnO (T–ZnO) also exhibited hexagonal-rod-shaped

arms of 200 nm thickness connected with a well-defined core forming a reasonable porous network. The Pd nanoparticles were uniformly distributed with minimal agglomeration observed along each facet of ZnO sensing materials. The majority of the Pd nanoparticles on the ZnO–NR films were observed on the hexagonal top facets of the nanorods, while the Pd nanoparticles were evenly dispersed along the arms and core in the case of T–ZnO. The XRD spectra shown in Figure 2C exhibit a polycrystalline structure in the sensor materials investigated. The reflection peaks identified are at $2\theta = 31.7°$, $34.4°$, $36.2°$, and $47.6°$, which correspond to lattice planes of (100), (002), (101), and (102), respectively, indexed to the hexagonal wurtzite ZnO structure (JCPDS Card No. 79-0206) [63]. The peaks at $2\theta = 39.86°$ and $46.6°$ are due to Pt interdigitated electrodes (IDE) indexed to (111) and Pd nanoparticles indexed to (200) phases. The corresponding lattice parameters are $c = 5.196$ Å and $a = 3.00$ Å for ZnO–NR_{150} films and $c = 5.20$ Å and $a = 3.02$ Å for T–ZnO_{250} films. For the Pdcat/ZnO–NR and Pdcat/T–ZnO films, the lattice parameters are $c = 5.20$ Å and $a = 3.03$ Å. The lattice parameter c value is consistent with the bulk values, while lattice parameter a and the c/a hexagonality ratio (1.715 ± 0.05) were within 7–9% of the bulk wurtzite (*ca.* $c = 5.206$ Å, $a = 3.249$ Å, $c/a = 1.602$). Likewise, Figure 2D shows room temperature PL spectra for ZnO–NR_{150} and T–ZnO_{250} thin films. ZnO possesses two emission peaks. One occurs at 375 nm in the UV region and the other band occurs between 480–560 nm in the visible region, which is typically broader due to defects (see Figure 2B schematic). The PL spectra for ZnO–NR and T–ZnO show a sharp peak in the UV region at 388 nm ($E_{ph} = 3.20$ eV), ascribed to near-band-edge emission of ZnO (ca. 3.37 eV) and free exciton recombination, as well as showing multiple smaller peaks in the 430–500 nm range and a broad peak at 600 nm [18,64,65]. The intensity of broad-band luminescence due to surface oxygen vacancies is greater for T–ZnO than that of ZnO–NR. Thus, T–ZnO can be more catalytically (re)active than vertically standing ZnO–NR of comparable size dimensions and have a higher propensity toward oxygen adsorption, gas reactivity, and desorption affecting the sensing performance demonstrated in this work. This difference also shows that they have a specific optimal detection temperature of 175 °C for ZnO–NR (Pd_{cat}/ZnO–NR) and 200 °C for T–ZnO (Pd_{cat}/T–ZnO), as revealed in Figure 3a, through electrical conductivity variation with temperature. This leads to a change in the electrical conductivity properties, which increases as the operating temperature is elevated because of the increase in electron density caused by thermal excitation in a semiconductor, followed by an increase due to oxygen adsorption on the nanostructured surface. Moreover, the operating temperature along with topological curvature is significant in the adsorption/desorption of methane (CH_4) gas molecules, since the adsorbed oxygen species at elevated temperatures and positive curvature of ZnO morphologies (cylindrical nanorod or nanoarm) are more reactive than those generated at lower temperatures and planar surfaces. We also investigated the electrical conductivity under UV excitation at lower temperatures (40–100 °C) and deduced the activation energy (E_A) following the Arrhenius formula summarized in Figure 3b. A thickness dependent study on ZnO films under UV illumination conducted by Su et al. demonstrated the highest sensitivity at ambient temperature and found that response to the target gas (NO_2) increased with increasing thickness to a maximum of 1500 nm, after which the response decreased [41]. They suggested that the thicker films possess higher levels of porosity, which had a larger penetration depth for UV light to create more photogenerated carriers and efficient diffusion of gas molecules.
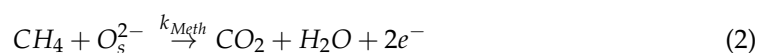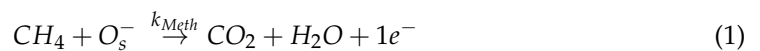
(a)

(b)
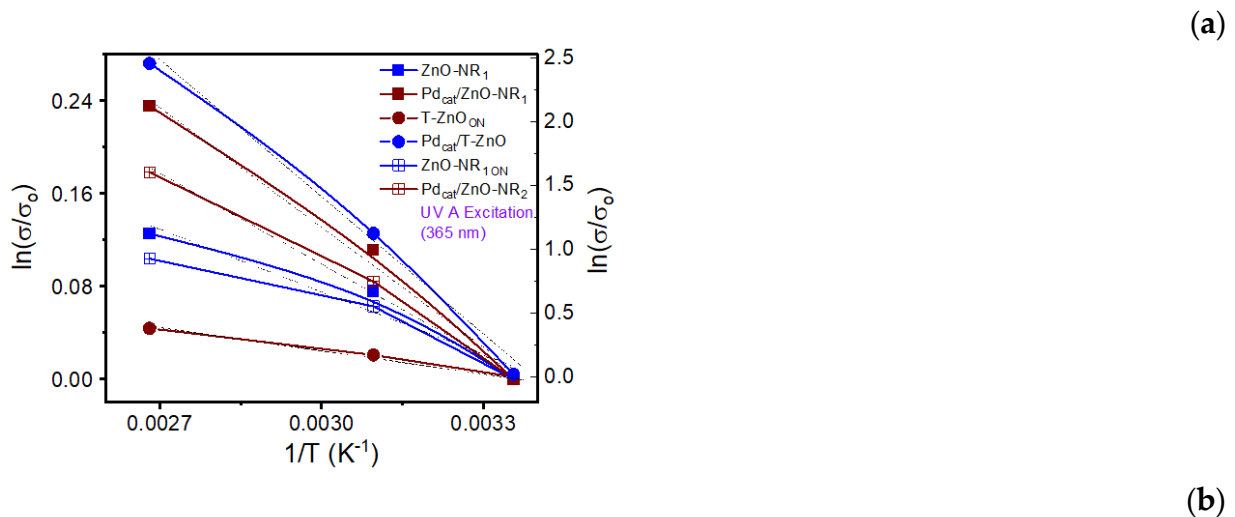
Sensor	E_A (eV)$_{Dark}$	E_A (eV)$_{UV\ A}$
ZnO–NR$_1$	0.31	0.024
Pd$_{cat}$/ZnO–NR$_1$	0.24	0.06
T–ZnO	0.51	0.10
Pd$_{cat}$/T–ZnO	0.54	0.09
ZnO–NR$_2$	0.32	0.17
Pd$_{cat}$/ZnO–NR$_2$	0.29	0.16

Figure 3. Optimization of operating temperature and activation energy. (**a**) Representative semilog plot of *dc* conductivity with temperature in the dark and with UV A excitation (365 nm) for ZnO–NR$_{1\ and\ 2}$, Pd$_{cat}$/ZnO–NR$_{1\ and\ 2}$, T–ZnO, and Pd$_{cat}$/T–ZnO sensor films measured in synthetic air. (**b**) Corresponding activation energy summary table. The short, dotted lines in (**a**) are the linear fits.

3.2. Conceptual Analytical Model for Methane Gas Sensing Mechanism

This section provides mathematical formulation of an analytical model based on the key concept behind the working principle of MOS-based gas sensors. The gas sensing response is a process caused by the interaction between analyte gas molecules and exposed faces of complex ZnO morphologies related to the chemisorbed oxygen on the ZnO surface. Briefly, at a low temperature (~100 °C), only molecular oxygen (O_2) is adsorbed on the semiconductor ZnO surface holding electrons from the conduction band, i.e., $O_{2g} + e^- \Leftrightarrow O^-_{2s}$. However, at higher temperatures, >100–400 °C, the ionized molecular O_2^- [$1/2 O_2 + e^- \xrightarrow{k_{oxy}} O_s^-$] and atomic oxygen O_s^-, O_s^{2-} [$1/2 O_2 + 2e^- \xrightarrow{k_{oxy}} O_s^{2-}$] can coexist [61]. Therefore, for ZnO-based methane sensors operating around 175–225 °C, the interaction between oxygen ions and gas molecule surface of *n*-type ZnO is used. When methane (CH$_4$, Meth) molecules interact with oxygen ions, the electrons are liberated and sent to the conduction band, which contributes to an increase in the electrical conductivity (i.e., decrease in resistance), also known as 'chemiresistors' and described by Equations (1) and (2) for O_s^- and O_s^{2-}, respectively, as follows:

$$CH_4 + O_s^- \xrightarrow{k_{Meth}} CO_2 + H_2O + 1e^- \tag{1}$$

$$CH_4 + O_s^{2-} \xrightarrow{k_{Meth}} CO_2 + H_2O + 2e^- \tag{2}$$

The rate equations for the electron density can be written as follows:

$$\frac{dn}{dt} = k_{Meth}(T) \left[O_s^-\right]^1 [CH_4]^1 \tag{3}$$

$$\frac{dn}{dt} = k_{Meth}(T) \left[O_s^{2-}\right]^{1/2} [CH_4]^{1/2} \tag{4}$$

or collectively,

$$\frac{dn}{dt} = k_{Meth}(T) \left[O_s^{ion}\right]^b [CH_4]^b \tag{5}$$

where n is the electron density, b = 1 for singly charged oxygen or ½ for doubly charged oxygen' $k_{Meth}(T)$ represents the reaction rate coefficient, which follows the Arrhenius behavior = A exp $(-E_a/k_BT)$, E_a is the activation energy of reaction, k_B is the Boltzmann constant, and T is the absolute temperature. Solving Equation (5), with n under methane gas, can be represented as follows:

$$n = k_{Meth}(T) \left[O_s^{ion}\right]^b [CH_4]^b t + n_0 \tag{6}$$

n_0 is the electron density in the air, and both carrier densities (n and n_0) are independent or constant of time at equilibrium. Thus, Equation (6) becomes the following:

$$n = \tau_r \, k_{Meth}(T) \left[O_s^{ion}\right]^b [CH_4]^b + n_0 \tag{7}$$

where τ_r is time constant and the carrier concentration n = $\frac{\alpha}{R'}$, which is in inverse relation with the resistance, R, and α is a proportionality factor. Substituting this behavior in Equation (6) gives Equation (8), as follows:

$$\frac{1}{R_g} = \frac{\tau_r \, k_{Meth}(T) \left[O_s^{ion}\right]^b [CH_4]^b}{\alpha} + \frac{1}{R_a} \tag{8}$$

The response magnitude is defined by $S_g = R_a/R_g$ (or I_g/I_a), where R_a (I_a) is the sensor resistance (current) in the air and R_g (I_g) is the resistance (current) under methane gas exposure. Note that the same approach can be used for the *pn*-junction or FET-type devices developed for gas sensors, as they measure current (I) instead of resistance (R). Thus,

$$S_g = \frac{R_a}{R_g} = \frac{\tau_r \, k_{Meth}(T) \left[O_s^{ion}\right]^b [CH_4]^b}{n_0} + 1 \tag{9}$$

Equation (10) can be rewritten in composite form relating to methane concentration [CH$_4$], C_g, as follows:

$$S_g = aC_g^b + 1 \tag{10}$$

where 'a' is a fitting parameter. Equation (11) can be rewritten as follows:

$$\log(S_g - 1) = \log a + b\log C_g \tag{11}$$

From this, a linear relation is apparent relating log ($S_g - 1$) versus log C_g with slope b, the value of which represents the oxygen ion species type on the surface of ZnO.

Typically, we attribute the enhancement of the physical properties of nanostructures to a higher surface-to-volume (S/V) ratio as one of the key factors, and especially when these nanomaterials are used as sensors that are related to porosity, enabling the diffusion of target gas molecules. In fact, the density of adsorbed oxygen ions is controlled by the S/V ratio of the nanostructures and, therefore, it should be included in Equation (10). The

following equation shows the direct dependence of adsorbed oxygen ion density on the S/V ratio:

$$\left[O_s^{ion}\right] = \frac{\sigma_0 \ (S/V) V_m}{V_s} \tag{12}$$

where σ_0 is the oxygen ion density, S/V is the surface-to-volume ratio of the material (V_m), and Vs is the system volume. The substitution of Equation (12) into Equation (9) gives S_g, as follows:

$$\left[O_s^{ion}\right] = \frac{\sigma_0 \left(\frac{S}{V}\right) V_m}{V_s} \tag{13}$$

$$S_{\left(\frac{S}{V} = \Phi\right)} = \frac{R_a}{R_g} = \frac{\tau_r \ k_{Meth}(T) \left[\frac{\sigma_0 \left(\frac{S}{V}\right) V_m}{V_s}\right]^b}{n_0} C_g^b + 1 \tag{14}$$

It is worth mentioning that the electrical property is changed through the redox state of the promoter and by donor (or acceptor) charges from gas molecules, which works on the principle of change in resistance upon exposure to analyte gas, known as 'chemiresistor' (see Figure 2A schematic). In other words, the decrease (or increase) in resistance of the MOS films depends upon the type of majority carriers (receptor function) in the semiconducting film and the nature of the gas molecules (reducing or oxidizing) in the synthetic atmosphere (air). For example, for *n*-type semiconducting materials, reducing gases (donor; CH_4, H_2, H_2S, CO, NH_3, VOC) decrease the resistance, while oxidizing gases (acceptor; NO_2, NO, SO_2) increase, and, correspondingly, converse behavior is observed for *p*-type semiconducting materials (transducer function) [66,67]. Thus, the receptor function (RED/OX) works together with the transduction function. Consequently, the adsorbed gas molecules interacting with molecular and atomic oxygen ionic sites on MOS surfaces regulate the response magnitude of the electrical signal induced by charge transfer from the surface to the bulk, which is proportional to the gas concentration (C_g) discussed in the analytical model.

3.3. Nanorod Diameter and Tetrapod Arm Thickness Dependent Analysis (Surface-to-Volume Ratios)

The impacts of nanorod diameter and the arm thickness of tetrapods on methane gas sensing performance are investigated by comparing gas sensors with different diameters and arm thicknesses, which are controlled by growth time (8–12 h) and high temperature treatment at 1100 °C for 4–8 h, respectively. The resulting diameters ranged between 50 nm, 150 nm, and 300 nm, and arm thickness between 70 nm, 250 nm, and 400 nm for the respective gas sensors. All the fabricated sensors have been evaluated at a range of temperatures (50–275 °C) to find the optimal working temperature discussed above to correspond to the morphology (see Figure 3). The operating temperature is an important parameter affecting performance while designing energy-saving chemiresistive sensors based on MOSs. We observed that the sensitivity toward methane for ZnO sensors increased with the operating temperature up to 175–200 °C, depending upon the morphology, and then decreased with a further increase in temperature [5,17,46]. This is because the ZnO sensors reach high enough thermal activation energy for sensing, as opposed to a low temperature. However, at very high temperatures the sensors are also less active, which can be attributed to desorption of methane gas molecules without an exchange of charges, meaning they are less sensitive and, therefore, an optimum working temperature is essential [5,17,46]. Additionally, in the wake of decreasing working temperature and the development of energy-saving chemiresistive gas sensors, the other approaches to decrease operating temperatures are UV photoactivation when combined with low temperature (~40–60 °C) activation and *pn*-diode-like junction devices working with depletion-assisted

enhanced sensitivity operating in reverse bias as opposed to high working temperatures (ca. 175–200 °C), as elucidated in our previous works [17,46]. Considering the use of the analytical model presented in this work, the activation methods are intertwined with the morphology and size and, therefore, it is indirectly related presented below. Nevertheless, this finding is significant for low power consumption "energy-saving" gas sensing devices rated at the maximum power of 100 mW/cm^2 (ca. 80 mW/cm^2) for sensors developed in this study [21].

Figure 4a shows methane sensing characteristics between 175 and 200 °C operating temperature for different gas concentration levels by showing plots of log $(S_g - 1)$ versus log C_g for ZnO–NR$_{150}$, Pdcat/ZnO–NR$_{150}$, T–ZnO$_{250}$, and Pdcat/T-ZnO$_{250}$ sensors, where a linear relationship described by Equation (10) is observed and slope b value represents the oxygen ion species (singly versus doubly charged). The values of b = 0.52, 0.62, 0.65, and 0.53–0.63 for ZnO–NR$_{150}$, Pd$_{cat}$/ZnO–NR$_{150}$, T–ZnO$_{250}$, and Pd$_{cat}$/T–ZnO$_{250}$ sensors, respectively, suggest that the $O_s{}^{2-}$ ions are the dominant adsorbed oxygen species at the surface of the investigated sensors. However, a marginal increase and decrease in b values for ZnO–NR and T–ZnO indicate the balance of $O_s{}^{2-}$ and $O_s{}^-$ species shifts, though coexist for both the sensors. This also suggests that the charged oxygen adsorption species on the surface is independent of grain size, regardless of bulk micro- or nanostructure. It is obvious that the diameter and arm thickness of ZnO–NR$_{150}$ and T–ZnO$_{250}$ are greater than the Debye length L_d of ~5–10 nm. Therefore, the impact of the surface charge region is limited, and the surface-to-volume ratio (S/V = Φ) of these nanostructures is expected to play a vital role in sensing performance, as represented in Equation (14) [60]. However, the deviation of b from its ideal value, 0.5—for which the diameter is close to Debye length $(2L_d)$—can also arise, because the surface depletion layer has some effect on the oxygen adsorption species at the ZnO surface. The dependence of sensitivity on the diameter of the nanorods and arm thickness of T–ZnO can be clarified by the surface-to-volume ratios and applying them in Equation (14) for the sensitivity ratios [64], as follows:

$$\frac{S_g(ZnO-NR_B)-1}{S_g(ZnO-NR_A)-1} = \left[\frac{(S/V)_B}{(S/V)_A}\right]^b = \left[\frac{D_A}{D_B}\right]^b \tag{15}$$

and

$$\frac{S_g(T-ZnO_A)-1}{S_g(T-ZnO_B)-1} = \left[\frac{(S/V)_A}{(S/V)_B}\right]^b = \left[\frac{Th_B}{Th_A}\right]^b \tag{16}$$

Table 1 summarizes a list of sensor formulae for methane gas sensors based on ZnO, which are also applicable to other MOSs. Tables 2 and 3 present the calculated response magnitude (sensitivity) ratios of each of the sensor morphologies studied with varying methane gas concentrations ([CH$_4$] = 100, 200, 300, 500, and 1000 ppm) and their experimental results, in addition to their Pd nanoparticles' decorated counterparts. Compared with their surface-to-volume ratios presented in the last row, reasonable agreement is noticed for the ZnO nanorod sensor. Therefore, it was concluded that the increase in surface-to-volume ratio enhances performance. Likewise, it is also clear that the increasing S/V ratio of the tested sensors improves the speed of the response/recovery times. However, the values for T-ZnO are significantly different by 65–73% for the experimental and calculated results, which required attention and calls for the modification and improvement of the analytical model, which is discussed below in relation to space-charge region (depletion layer width).
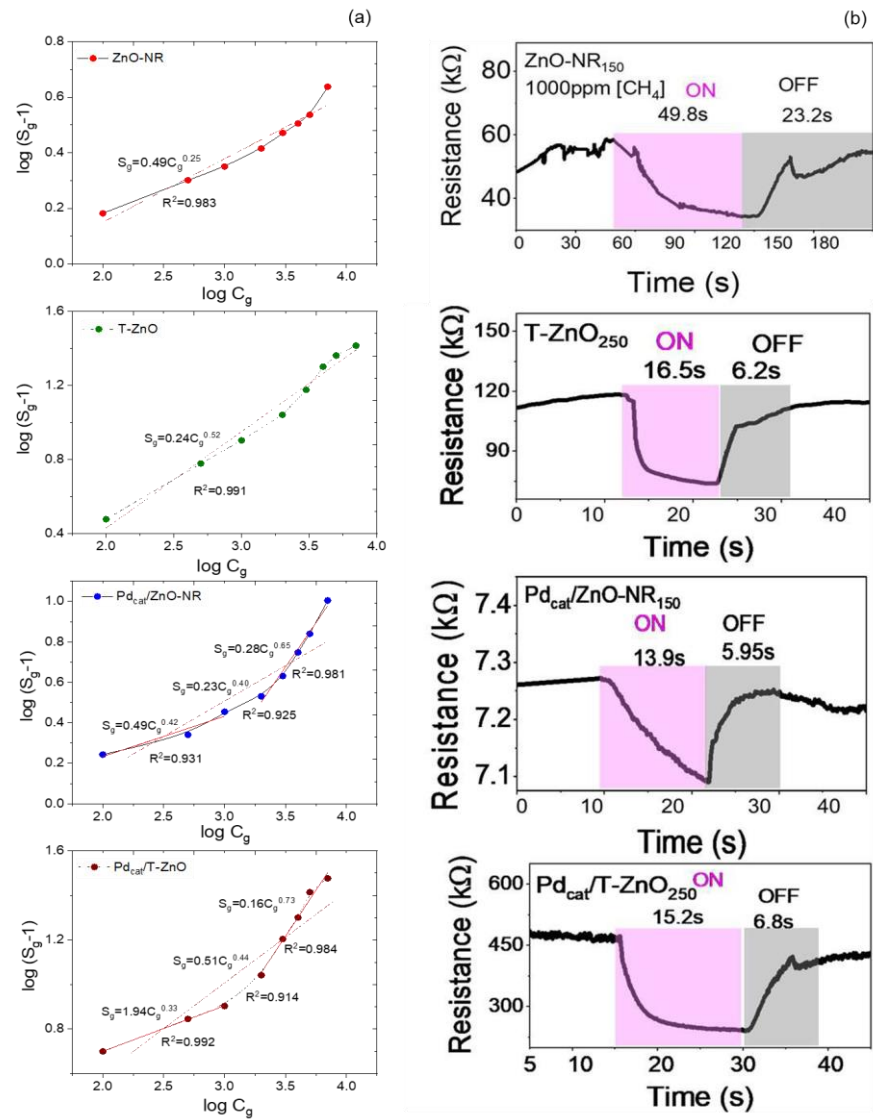
Figure 4. Performance of methane sensing from nanostructured ZnO. (**a**) log ($S_g - 1$) versus log C_g plot and (**b**) response/recovery curves to 1000 ppm concentration of methane [CH_4] at 175 °C for ZnO–NR, Pdcat/ZnO–NR, and at 150 °C for T–ZnO and Pdcat/T–ZnO sensors.

Table 1. Summary of sensor response magnitude formulae for methane gas sensors based on ZnO nanostructures and applicability towards factors considered to be influencing their behavior (adapted from ref. [58]).

Sensor Response Formulae	Oxygen ion Species	Metal Doping/Schottky Behavior	Nanostructure when $D > 2L_d$	Nanostructure when $D \sim 2L_d$
$S_g = aC_g^b + 1$	√	X	X	X
$S_g = \dfrac{\tau_r \, k_{Meth}(T) \left[O_s^{ion}\right]^b}{n_0} C_g^b + 1$	√	√	X	X
$S_{\frac{S}{V}=\Phi} = \dfrac{\tau_r \, k_{Meth}(T) \left(\sigma_0 \, \Phi\left(\frac{V_m}{V_s}\right)\right)^b}{n_0} C_g^b + 1$	√	√	√	X
$S_{L_d} = \left(\dfrac{\tau_r \, k_{Meth}(T)\left(\sigma_0 \, \Phi\left(\frac{V_m}{V_s}\right)\right)^b}{n_0}\right) \dfrac{D^2 C_g^b}{(D - 2L_d)^2} + 1$ or $S_{L_d} = \left(\dfrac{\tau_r \, k_{Meth}(T)\left(\sigma_0 \, \Phi\left(\frac{V_m}{V_s}\right)\right)^b}{n_0}\right) \dfrac{Th \, C_g^b}{(Th - 2L_d)} + 1$	√	√	√	√

Note: √ = Applicable, X = Not Applicable.

Table 2. Response magnitude ratios of ZnO–NR (nanorods) of various sizes with methane concentration compared with the calculated values.

Methane Concentration	Response Magnitude Ratios			
	$\frac{S_g(ZnO-NR_{50})-1}{S_g(ZnO-NR_{100})-1}$	$\frac{S_g(ZnO-NR_{50})-1}{S_g(ZnO-NR_{150})-1}$	$\frac{S_g(ZnO-NR_{50})-1}{S_g(ZnO-NR_{300})-1}$	$\frac{S_g(Pd_{cat}/ZnO-NR_{50})-1}{S_g(Pd_{cat}ZnO-NR_{150})-1}$
100 ppm	1.239	1.639	2.339	1.659
200 ppm	1.241	1.648	2.368	1.673
300 ppm	1.253	1.673	2.423	1.682
500 ppm	1.388	1.718	2.448	1.728
1000 ppm	1.421	1.741	2.451	1.731
$[D_A/D_B]^{1/2}$	1.414	1.732	2.449	1.732

Table 3. Response magnitude ratios of T-ZnO (tetrapods) of varying arm thicknesses with methane gas concentration compared with the calculated values from two models.

Methane Concentration	Response Magnitude Ratios			
	$\frac{S_g(T-ZnO_{70})-1}{S_g(T-ZnO_{250})-1}$	$\frac{S_g(T-ZnO_{70})-1}{S_g(T-ZnO_{400})-1}$	$\frac{S_g(T-ZnO_{250})-1}{S_g(T-ZnO_{400})-1}$	$\frac{S_g(Pd_{cat}/T-ZnO_{70})-1}{S_g(Pd_{cat}/T-ZnO_{400})-1}$
100 ppm	4.320	5.451	4.350	4.216
200 ppm	4.457	5.843	5.124	4.392
300 ppm	5.346	5.964	5.589	4.450
500 ppm	5.852	6.359	5.832	4.477
1000 ppm	5.873	6.372	5.945	5.012
$[Th_B/Th_A]^{1/2}$	1.890	2.390	1.265	2.390
$[Th_B/Th_A]^{\frac{1}{2}}\left(\frac{Th_A}{Th_A-2L_d}\right)\left(\frac{Th_B-2L_d}{Th_B}\right)$	5.123	5.267	3.987	4.891

3.4. Depletion Layer Width Dependence (Surface-Charge-Region Model)

According to the SCR model, the surface electronic property is characterized by the depletion layer width, presented as follows [55]:

$$W = L_d \left(eV_s/k_BT\right)^{1/2} \tag{17}$$

$$W = \left(2\varepsilon_s(V_{bi} - V - k_BT/e)/eN_D\right)^{1/2} \tag{18}$$

where L_d is the Debye length and V_s is band bending induced by adsorbates and Pd nanoparticles making local Schottky contacts, V the applied bias, and V_{bi} is the barrier voltage. The Debye length is used to scale the depletion region of the nanostructured ZnO. The following equation is used to calculate the Debye length, L_d:

$$L_d = \left[\frac{\varepsilon\varepsilon_0 k_BT}{e^2 n}\right]^{1/2} \tag{19}$$

where ε is the relative dielectric permittivity of the ZnO nanostructure and n is the charge carrier density. The calculated Debye length obtained by using electron density (ranged 10^{17}–10^{18} cm^{-3}), T = 573 °K (optimum working temperature), $\varepsilon_s = \varepsilon\varepsilon_0 = 7.9 \times 8.85 \times 10^{-12}$ F.m^{-1} yielding L_d of about 5.2 nm for n = 8×10^{17} cm^{-3}, which is lower than the values reported in the literature, with about 30 nm [68–71]. Since the value of $2L_d$ = 10.4 nm, it is suspected that the reason behind the observed significant variation is far from the diameter and thickness of ZnO–NR and T–ZnO. Therefore, a modification is applied to the model considering the S/V ratio and the width of the depletion layer region. At a distance that is equal to many times that of the Debye length from the surface of ZnO nanomaterials, the carriers'

density is equal to the bulk value. Therefore, for large enough ZnO sizes ($>>2L_d$), bulk characteristics can be assumed. It is clear L_d increases with temperature and decays with growing density of donor defects. When exposed to analyte methane, the molecules react with surface oxygen ion species and give back electrons to ZnO, resulting in an increased conductive channel (or decreased depletion layer). The conductive channel is related to the carrier concentration and can be written in terms of L_d, as follows:

$$n' = n_0 \, \frac{\pi(D - 2L_d)^2}{\pi D^2} \tag{20}$$

or

$$n' = n_0 \, \frac{(Th - 2L_d)}{Th} \tag{21}$$

where n_0 is the intrinsic carrier concentration and D is the diameter of the 'cylindrical' nanorod (or tetrapod arm). The depletion layer effects on sensor response based on cylindrical ZnO nanostructures with a surface-to-volume ratio parameter (Φ) is given as follows:

$$S_{L_d} = \frac{R_a}{R_g} = \left(\frac{\tau_r \, k_{Meth}(T) \left[\sigma_o \Phi \left(\frac{V_m}{V_s} \right) \right]^b}{n_0} \right) \frac{D^2 C_g^b}{(D - 2L_d)^2} + 1 \tag{22}$$

or

$$S_{L_d} = \frac{R_a}{R_g} = \left(\frac{\tau_r \, k_{Meth}(T) \left[\sigma_o \Phi \left(\frac{V_m}{V_s} \right) \right]^b}{n_0} \right) \frac{Th \, C_g^b}{(Th - 2L_d)} + 1 \tag{23}$$

Thus, the final influence of the S/V ratio and depletion region on sensitivity ratios based on varying diameters and arm thicknesses are presented as follows:

$$\frac{S_g(ZnO - NR_B) - 1}{S_g(nO - NR_A) - 1} = \left[\frac{(S/V)_A}{(S/V)_B} \right]^b \left(\frac{D_B}{D_B - 2L_d} \right)^2 \left(\frac{D_A - 2L_d}{D_A} \right)^2 = \left[\frac{D_B}{D_A} \right]^{1/2} \left(\frac{D_B}{D_B - 2L_d} \right)^2 \left(\frac{D_A - 2L_d}{D_A} \right)^2 \tag{24}$$

and

$$\frac{S_g(T - ZnO_A) - 1}{S_g(T - ZnO_B) - 1} = \left[\frac{(S/V)_A}{(S/V)_B} \right]^b \left(\frac{Th_A}{Th_A - 2L_d} \right) \left(\frac{Th_B - 2L_d}{Th_B} \right) = \left[\frac{Th_B}{Th_A} \right]^{1/2} \left(\frac{Th_A}{Th_A - 2L_d} \right) \left(\frac{Th_B - 2L_d}{Th_B} \right) \tag{25}$$

The calculated sensitivity ratios and experimental results are presented for the sensors shown in Table 3. It is evident that after consideration of the depletion region, the calculated results have much better agreement with the experimental results for all cases. The subsequent difference between the calculated and experimental measurements is 10–12%. It is interesting to note that the sensitivity for T–ZnO is significantly enhanced compared to that of ZnO–NR, since the diameter or the interconnected arm thickness is closer to 50 nm or 70 nm. Figure 4b shows the response/recovery time for the representative sensors (ZnO–NR$_{150}$, T–ZnO$_{250}$, Pdcat/ZnO–NR$_{150}$, and Pdcat/ZnO–NR$_{250}$) studied in this work to 1000 ppm of [CH$_4$], which is 49.8 s/23.2 s, 16.5 s/6.2 s, 13.9 s/6.2 s, and 15.2 s/6.8 s, respectively. The decrease in response time is explained by the complete coverage of the sensor surface by methane gas molecules and the mean residence time of the gas molecules. At low concentrations, the reaction between the target gas molecules and the oxygen ion species occurs over a relatively long period of time, which shows the response behavior; moreover, and at a higher concentration, the time needed for the reaction is decreased, causing the response time to be shorter, especially for T–ZnO compared to ZnO–NR, which is also influenced by Pd nanoparticles. It is important to note that the initial surface of both

ZnO–NR and T–ZnO sensors is restored after keeping them in air at 175 °C for 15 min or at room temperature for 12–20 h, indicative of reproducibility due to faster desorption of the target gas species and stability.

3.5. Effect of Surface Chemical-Electronic Sensitization (Noble Metal Nanoparticle Decoration)

It is known that doping in semiconductors modifies the electronic properties such that it affects the sensor response as well [17]. The metal doping effect can be simply explained in the model by Equation (13). It is seen that the average sensor response is proportional to the reaction rate constants, $k_{\mathrm{Meth}}(T)$ and $k_{\mathrm{Oxy}}(T)$, through oxygen density. It has also shown that the reaction rate constant can be affected by noble metal decoration, such that Pd on the semiconductor oxide sensor promotes a surface catalytic effect and Schottky behavior, leading to local doping effects. Thus, metal doping causes increased reaction rate constants elucidated by increasing resistance in the air suggestive of catalytically active dissociation of molecular oxygen, resulting in increased molecular oxygen adsorption. Therefore, an electron in the ZnO nanostructure is captured by oxygen adsorption to form an oxygen ion and, hence, the ZnO nanostructure loses more electrons, which causes increased depletion layer width and higher resistance, which is overcome by thermal and UV activation keeping an enhanced sensitivity, as observed here in this study, despite the contrary effect. Moreover, chemical-electronic sensitization proposed by Yamazoe [66] facilitating Schottky contacts motivated the need to achieve a lower operating temperature, faster response/recovery time, effective gas diffusion/adsorption, and photocatalytic oxidation (see also refs. [15,67]). See also Figure 5, which summarizes the sensing material properties affecting the sensor response and corresponding gas sensing mechanisms for metal oxide semiconductors with specifics to ZnO nanostructures.
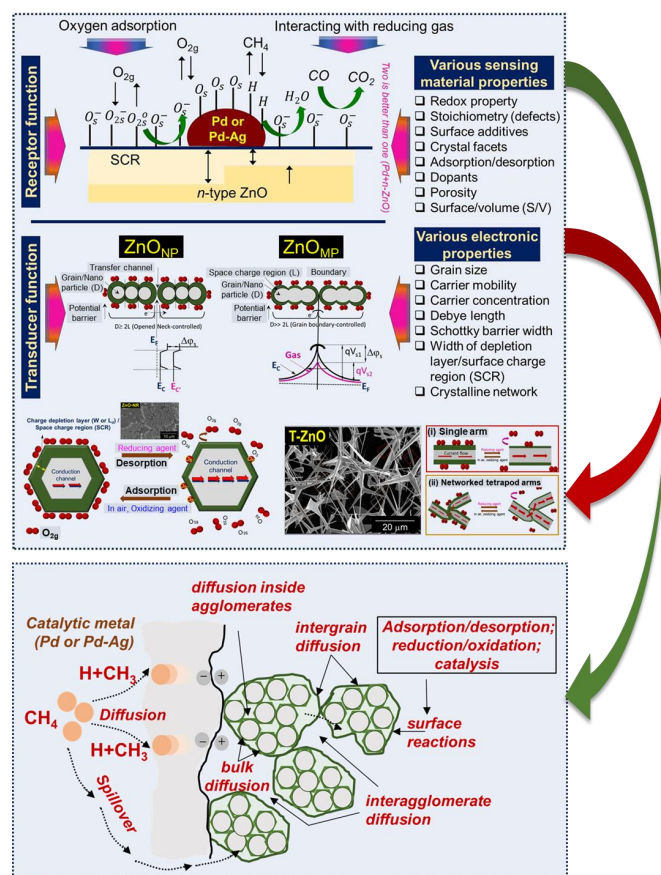

Figure 5. Material properties and schematics of gas sensing mechanisms. Receptor function, transducer function, physicochemical, and material properties of MOS (specifically ZnO) gas sensors listed on the

right. The detailed sensing process is shown as a space-charge region model related to surface oxygen ion species describing oxygen adsorption on unsensitized and chemical-electronic sensitized surface with Pd (or Pd–Ag) nanoparticles and band-bending theory. Also shown is a schematic illustrating processes limiting (or enhancing) the kinetics of gas diffusion while inducing surface dipoles, as well as spillover on sensitized ZnO nanorods assembly, nanostructured surface.

4. Conclusions

In summary, gas sensors based on ZnO-aggregated nanostructures with two different controlled morphologies, including nanorods of different diameters and topology interconnected tetrapods with varying arm thicknesses synthesized through low-temperature chemical solution and flame transport methods, respectively, are investigated. Moreover, methane gas transduction mechanisms illustrating the relationships between the surface adsorption phenomenon and the resulting electrical property effects, as well as surface chemical sensitization, are presented. Methane gas sensors were fabricated as MEMS-like devices based on sparse ZnO-based nanostructures, and their performance was compared alongside the implementation of an analytical model for a better understanding of the mechanistic pathways. Smaller diameter nanorods and thinner tetrapod arm thicknesses, yet interconnected, having higher surface-to-volume ratios elucidates enhanced sensitivity, low detection limit, and faster response/recovery characteristics toward methane gas. Moreover, a tetrapod arm thickness closer to or comparable with the thickness of the ZnO depletion layer showed significantly increased sensitivity attributed to the semi-complete depletion layer formed by the nanoarm connectivity. The explanation of the results is based on the formulation established by considering the chemical reaction between methane gas molecules and adsorbed oxygen ions contributing to depletion layer thickness. The generalized formula has significant potential for designing sensors with any desired sensitivity, especially at the ppb (parts per billion) level of concentration and in the development of an "electronic nose" for environmental and toxic industrial gases. This work can be generalized to other metal oxides (SnO_2, MoO_3, Cu_2O, and WO_3) as potential sensing materials to detect different active gases (CO_2, NO_x, NH_3, H_2S, and VOC). Finally, ultraviolet light activation in combination with thermal activation promoted the detection of methane gas at lower temperatures, and the relationship between response and light intensity may further strengthen the persuasive conclusion.

References

1. Bačėninaitė, D.; Džermeikaitė, K.; Antanaitis, R. Global Warming and Dairy Cattle: How to Control and Reduce Methane Emission. *Animals* **2022**, *12*, 2687. [CrossRef] [PubMed]
2. Santhanam, K.; Ahamed, N. Greenhouse Gas Sensors Fabricated with New Materials for Climatic Usage: A Review. *Chemengineering* **2018**, *2*, 38. [CrossRef]
3. U.S. Environmental Protection Agency. Overview of Greenhouse Gases. 2022. Available online: https://www.epa.gov/ghgemissions/overview-greenhouse-gases (accessed on 15 May 2022).
4. Neethirajan, S. Transforming the Adaptation Physiology of Farm Animals through Sensors. *Animals* **2020**, *10*, 1512. [CrossRef]
5. Knoepfel, A.; Liu, N.; Hou, Y.; Sujani, S.; dos Reis, B.R.; White, R.; Wang, K.; Poudel, B.; Gupta, S.; Priya, S. Development of tetrapod zinc oxide-based UV sensor for precision livestock farming and productivity. *Biosensors* **2022**, *12*, 837. [CrossRef] [PubMed]
6. Thompson, A.M.; Hogan, K.B.; Hoffman, J.S. The Oxidizing Capacity of the Earth's Atmosphere: Probable Past and Future Changes. *Atmos. Environ. Part A Gen. Top.* **1992**, *26*, 2665–2668.
7. Tham, K.W. Indoor air quality and its effects on humans—A review of challenges and developments in the last 30 years. *Energy Build.* **2016**, *130*, 637–650. [CrossRef]
8. Song, Y.G.; Kim, G.S.; Ju, B.-K.; Kang, C.-Y. Design of Semiconducting Gas Sensors for Room-Temperature Operation. *J. Sens. Sci. Technol.* **2020**, *29*, 1–6. [CrossRef]
9. Fu, L.; You, S.; Li, G.; Li, X.; Fan, Z. Application of Semiconductor Metal Oxide in Chemiresistive Methane Gas Sensor: Recent Developments and Future Perspectives. *Molecules* **2023**, *28*, 6710. [CrossRef] [PubMed]
10. Neri, G.; Donato, N. Resistive Gas Sensors. In *Wiley Encyclopedia of Electrical and Electronics Engineering*; Webster, J.G., Ed.; Wiley-Interscience: Hoboken, NJ, USA, 2016.
11. Ji, W.; Zeng, Y.; Li, Y. Gas sensing mechanisms of metal oxide semiconductors: A focus review. *Nanoscale* **2019**, *11*, 22664–22684. [PubMed]
12. Kumar, R.; Liu, X.; Zhang, J.; Kumar, M. Room-Temperature Gas Sensors Under Photoactivation: From Metal Oxides to 2D Materials. *Nano-Micro Lett.* **2020**, *12*, 164–167. [CrossRef]
13. Williams, D.E. Semiconducting oxides as gas-sensitive resistors. *Sensors Actuators B Chem.* **1999**, *57*, 1–16. [CrossRef]
14. Nikolic, M.V.; Milovanovic, V.; Vasiljevic, Z.Z.; Stamenkovic, Z. Semiconductor Gas Sensors: Materials, Technology, Design, and Application. *Sensors* **2020**, *20*, 6694. [CrossRef] [PubMed]
15. Bulemo, P.M.; Cheong, J.Y. Review on Porosity Control in Nanostructured Semiconducting Metal Oxides and Its Influence on Chemiresistive Gas Sensing. *ACS Appl. Nano Mater.* **2023**, *6*, 1027–1049. [CrossRef]
16. Bhati, V.S.; Hojamberdiev, M.; Kumar, M. Enhanced sensing performance of ZnO nanostructures-based gas sensors: A review. *Energy Rep.* **2019**, *6*, 46–62. [CrossRef]
17. Gupta, S.; Knoepfel, A.; Zou, H.; Ding, Y. Investigations of methane gas sensor based on biasing operation of n-ZnO nanorods/p-Si assembled diode and Pd functionalized Schottky junctions. *Sens. Actuators B Chem.* **2023**, *392*, 134030. [CrossRef]
18. Zhang, B.; Wang, J.; Wei, Q.; Yu, P.; Zhang, S.; Xu, Y.; Dong, Y.; Ni, Y.; Ao, J.; Xia, Y. Visible Light-Induced Room-Temperature Formaldehyde Gas Sensor Based on Porous Three- Dimensional ZnO Nanorod Clusters with Rich Oxygen Vacancies. *ACS Omega* **2022**, *7*, 22861–22871. [CrossRef] [PubMed]
19. Wang, J.; Hu, C.; Xia, Y.; Zhang, B. Mesoporous ZnO nanosheets with rich surface oxygen vacancies for UV-activated methane gas sensing at room temperature. *Sensors Actuators B Chem.* **2021**, *333*, 129547. [CrossRef]
20. Abdelhakim, H.K.; El-Sayed, E.R.; Rashidi, F.B. Biosynthesis of zinc oxide nanoparticles with antimicrobial, anticancer, antioxidant and photocatalytic activities by the endophytic Alternaria tenuissima. *J. Appl. Microbiol.* **2020**, *128*, 1634–1646. [CrossRef]
21. Majhi, S.M.; Mirzaei, A.; Kim, H.W.; Kim, S.S.; Kim, T.W. Recent advances in energy-saving chemiresistive gas sensors: A review. *Nano Energy* **2021**, *79*, 105369.
22. Wang, Z.L.; Zou, H.; Wang, L. *Nanowires and Nanotubes in Encyclopedia of Applied Physics*; Wiley-VCH GmbH: Weinheim, Germany, 2022. [CrossRef]
23. Basu, P.K.; Saha, N.; Jana, S.K.; Saha, H.; Spetz, A.L.; Basu, S. Schottky junction methane sensors using electrochemically grown nanocrystalline-nanoporous ZnO thin films. *J. Sens.* **2009**, *2009*, 790476. [CrossRef]
24. Tian, Z.R.; Voigt, J.A.; Liu, J.; Mckenzie, B.; Mcdermott, M.J.; Rodriguez, M.A.; Konishi, H.; Xu, H. Complex and oriented ZnO nanostructures. *Nat. Mater.* **2003**, *2*, 821–826. [CrossRef]
25. Zheng, K.H.; Zhao, Y.C.; Deng, K.; Liu, Z.; Sun, L.F.; Zhang, Z.X.; Song, L.; Yang, H.F.; Gu, C.Z.; Xie, S.S. Effectively enhanced oxygen sensitivity of individual ZnO tetrapod sensor by water pre-adsorption. *Appl. Phys. Lett.* **2008**, *92*, 213116–213118. [CrossRef]
26. Mishra, Y.K.; Adelung, R. ZnO Tetrapod Materials for Functional Applications. *Mater. Today* **2018**, *21*, 631–651. [CrossRef]
27. Comini, E.; Baratto, C.; Faglia, G.; Ferroni, M.; Vomiero, A.; Sberveglieri, G. Quasi- one-dimensional metal oxide semiconductors: Preparation, characterization, and application as chemical sensors. *Prog. Mater Sci.* **2009**, *54*, 1–136. [CrossRef]

28. Mishra, Y.K.; Modi, G.; Cretu, V.; Postica, V.; Lupan, O.; Reimer, T.; Paulowicz, I.; Hrkac, V.; Benecke, W.; Kienle, L.; et al. Direct Growth of Freestanding ZnO Tetrapod Networks for Multifunctional Applications in Photocatalysis, UV Photodetection, and Gas Sensing. *ACS Appl. Mater. Interfaces* **2015**, *7*, 14303–14316. [CrossRef] [PubMed]

29. Izyumskaya, N.; Avrutin, V.; Özgür, Ü.; Alivov, Y.L.; Morkoç, H. Preparation and properties of ZnO and devices. *Phys. Stat. Soldi b* **2007**, *244*, 1439–1450. [CrossRef]

30. Wyckoff, R.W.G. *Crystal Structures*, 2nd ed.; Interscience Publishers: Geneva, Switzerland, 1963; pp. 7–83.

31. Look, D.C.; Hemsky, J.W.; Sizelove, J.R. Residual native shallow donor in ZnO. *Phys. Rev. Lett.* **1999**, *82*, 2552–2555. [CrossRef]

32. Janotti, A.; de Walle, C.G.V. Native point defects in ZnO. *Phys. Rev. B* **2007**, *76*, 165202. [CrossRef]

33. Özgür, Ü.; Alivov, Y.I.; Liu, C.; Teke, A.; Reshchikov, M.A.; Doğan, S.; Avrutin, V.; Cho, S.-J.; Morkoç, H. A comprehensive review of ZnO materials and devices. *J. Appl. Phys.* **2005**, *98*, 041301. [CrossRef]

34. Razeghi, M.; Rogalski, A. Semiconductor Ultraviolet Detectors. *J. Appl. Phys.* **1996**, *79*, 7433–7473. [CrossRef]

35. Soci, C.; Zhang, A.; Xiang, B.; Dayeh, S.A.; Aplin, D.P.R.; Park, J.; Bao, X.Y.; Lo, Y.H.; Wang, D. ZnO Nanowire UV Photodetectors with High Internal Gain. *Nano Lett.* **2007**, *7*, 1003–1009. [CrossRef] [PubMed]

36. Bedia, A.; Bedia, F.; Aillerie, M.; Maloufi, N.; Benyoucef, B. Morphological and Optical Properties of ZnO Thin Films Prepared by Spray Pyrolysis on Glass Substrates at Various Temperatures for Integration in Solar Cell. *Energy Procedia* **2015**, *74*, 529–538. [CrossRef]

37. Vinitha, V.; Preeyanghaa, M.; Vinesh, V.; Dhanalakshmi, R.; Neppolian, B.; Sivamurugan, V. Two is better than one: Catalytic, sensing, and optical applications of doped zinc oxide nanostructures. *Emergent Mater.* **2021**, *4*, 1093–1124. [CrossRef]

38. Lupan, O.; Postica, V.; Gröttrup, J.; Mishra, A.K.; de Leeuw, N.H.; Adelung, R. Enhanced UV and ethanol vapor sensing of a single 3-D ZnO tetrapod alloyed with Fe_2O_3 nanoparticles. *Sens. Actuators B* **2017**, *245*, 448–461. [CrossRef]

39. Roy, S.; Das, S.; Sarkar, C.K. Investigation of nanostructured Pd-Ag/n-ZnO thin film based Schottky junction for methane sensing. *Int. Nano Lett.* **2016**, *6*, 199–210. [CrossRef]

40. Kolmakov, A.; Klenov, D.O.; Lilach, Y.; Stemmer, S.; Moskovits, M. Enhanced gas sensing by individual SnO2 nanowires and nanobelts functionalized with Pd catalyst particles. *Nano Lett.* **2005**, *5*, 667–673. [CrossRef] [PubMed]

41. Su, X.; Duan, G.; Xu, Z.; Zhou, F.; Cai, W. Structure, and thickness-dependent gas sensing responses to NO_2 under UV irradiation for the multilayered ZnO micro/nanostructured porous, thin films. *J. Colloid Interface Sci.* **2017**, *503*, 150–158. [CrossRef]

42. Xu, C.; Tamaki, J.; Miura, N.; Yamazoe, N. Grain size effects on gas sensitivity of porous SnO_2-based elements. *Sens. Actuat. B* **1991**, *3*, 147–155. [CrossRef]

43. Seiyama, T.; Kato, A.; Fujiishi, K.; Nagatani, M. A new detector for gaseous components using semiconductive thin films. *Anal. Chem.* **1962**, *34*, 1502–1503. [CrossRef]

44. Jaaniso, R.; Tan, O.K. *Semiconductor Gas Sensors*; Woodhead Publishing Limited: Cambridge, UK, 2013.

45. Yamazoe, N.; Fuchigami, J.; Kishikawa, M.; Seiyama, T. Interactions of Tin Oxide Surface with O_2, H_2O, and H_2. *Surf. Sci.* **1979**, *86*, 335–344. [CrossRef]

46. Knoepfel, A.; Poudel, B.; Gupta, S. Surface-Catalyzed Zinc Oxide Nanorods and Interconnected Tetrapods as Efficient Methane Gas Sensing Platforms. *Chemosensors* **2023**, *11*, 506. [CrossRef]

47. Wang, Y.; Meng, X.; Yao, M.; Sun, G.; Zhang, Z. Enhanced CH_4 sensing properties of Pd modified ZnO nanosheets. *Ceram. Int.* **2019**, *45*, 13150–13157. [CrossRef]

48. Ghosh, S.; RoyChaudhuri, C.; Bhattacharya, R.; Saha, H.; Mukherjee, N. Palladium- silver-activated ZnO surface: Highly selective methane sensor at reasonably low operating temperature. *ACS Appl. Mater. Interfaces* **2014**, *6*, 3879–3887. [CrossRef] [PubMed]

49. Zhang, S.; Li, H.; Zhang, N.; Zhao, X.; Zhang, Z.; Wang, Y. Self-sacrificial templated formation of ZnO with decoration of catalysts for regulating CO and CH_4 sensitive detection. *Sens. Actuators B Chem.* **2020**, *330*, 129286. [CrossRef]

50. Aghagoli, Z.; Ardyanian, M. Synthesis and study of the structure, magnetic, optical and methane gas sensing properties of cobalt doped zinc oxide microstructures. *J. Mater. Sci. Mater. Electron.* **2018**, *29*, 7130–7141. [CrossRef]

51. Mondal, B.; Dutta, L.; Roychaudhury, C.; Mohanta, D.; Mukherjee, N.; Saha, H. Effect of Annealing Temperature on the Morphology and Sensitivity of the Zinc Oxide Nanorods-Based Methane Sensor. *Acta Met. Sin.* **2014**, *27*, 593–600. [CrossRef]

52. Musa, I.; Qamhieh, N.; Mahmoud, S.T. Synthesis, and length dependent photoluminescence property of zinc oxide nanorods. *Results Phys.* **2017**, *7*, 3552–3556. [CrossRef]

53. Feng, P.; Wan, Q.; Wang, T.H. Contact-controlled sensing properties of flowerlike ZnO nanostructures. *Appl. Phys. Lett.* **2005**, *87*, 213111. [CrossRef]

54. Li, C.C.; Du, Z.F.; Li, L.M.; Yu, H.C.; Wan, Q.; Wang, T.H. Surface-depletion controlled gas sensing properties of ZnO nanorods grown at room temperature. *Appl. Phys. Lett.* **2007**, *91*, 032101. [CrossRef]

55. Sysoev, V.V.; Button, B.K.; Wepsiec, K.; Dmitriev, S.; Kolmakov, A. Toward the Nanoscopic "Electronic Nose": Hydrogen vs Carbon Monoxide Discrimination with an Array of Individual Metal Oxide Nano- and Mesowire Sensors. *Nano Lett.* **2006**, *6*, 1584–1588. [CrossRef]

56. Yuan, Q.; Zhao, Y.P.; Li, L.; Wang, T. Ab inito study of ZnO-based gas-sensing mechanisms: Surface reconstruction and charge transfer. *J. Phys. Chem. C* **2009**, *113*, 6107–6113. [CrossRef]

57. Shankar, P.; Rayappan, J.B.B. Gas sensing mechanism of metal oxides: The role of ambient atmosphere, type of semiconductor and gases—A review. *Sci. Lett. J.* **2015**, *4*, 126.

58. Cheng, J.; Hu, D.; Yao, A.; Gao, Y.; Asadi, H. A computational study on the Pd- decorated ZnO nanocluster for H_2 gas sensing: A comparison with experimental results. *Phys. E* **2020**, *124*, 114237. [CrossRef]

59. Liangruksa, M.; Laomettachit, T.; Siriwong, C. Enhancing gas sensing properties of novel palladium-decorated zinc oxide surface: A first-principles study. *Mater. Res. Express* **2021**, *8*, 045004. [CrossRef]

60. Hongsith, N.; Wongrat, E.; Kerdcharoen, T.; Choopun, S. Sensor response formula for sensor based on ZnO nanostructures. *Sens. Actuators B* **2010**, *144*, 67–72. [CrossRef]

61. Hong, T.; Culp, J.T.; Kim, K.-J.; Devkota, J.; Sun, C.; Ohodnicki, P.R. State-of-the-art methane sensing materials: A review and perspectives. *TrAC Trends Anal. Chem.* **2020**, *125*, 115820. [CrossRef]

62. Vayssieres, L. Growth of arrayed nanorods and nanowires of ZnO from aqueous solutions. *Adv. Mater.* **2003**, *15*, 464–466. [CrossRef]

63. Yogamalar, R.; Srinivasan, R.; Vinu, A.; Ariga, K.; Bose, A.C. X-ray peak broadening analysis in ZnO nanoparticles. *Solid State Commun.* **2009**, *149*, 1919–1923. [CrossRef]

64. Melnick, D.A. Zinc Oxide Photoconduction, an Oxygen Adsorption Process. *J. Chem. Phys.* **1957**, *26*, 1136–1146. [CrossRef]

65. Alenezi, M.R.; Alshammari, A.S.; Jayawardena, K.D.G.I.; Beliatis, M.J.; Henley, S.J.; Silva, S.R.P. Role of the UV activated ZnO nanostructured gas sensors. *J. Phys. Chem. C* **2013**, *117*, 17850–17858. [CrossRef] [PubMed]

66. Yamazoe, N. New approaches for improving semiconductor gas sensors. *Sensors Actuators B* **2001**, *5*, 7–19. [CrossRef]

67. Helwig, A.; Müller, G.; Sberveglieri, G.; Faglia, G. Gas response times of nano-scale SnO_2 gas sensors as determined by the moving gas outlet technique. *Sensors Actuators B Chem.* **2007**, *126*, 174–180. [CrossRef]

68. Grossner, U.; Christensen, J.S.; Svensson, B.G. Carrier concentration and shallow electron states in in-doped hydrothermally grown ZnO. *Superlattices Microstruct.* **2005**, *38*, 364–368. [CrossRef]

69. Bykhovski, A.D.; Kaminski, V.V.; Shur, M.S.; Chen, Q.C.; Khan, M.A. Pyroelectricity in gallium nitride thin films. *Appl. Phys. Lett.* **1996**, *69*, 3254–3256. [CrossRef]

70. Varshni, Y. Temperature dependence of the energy gap in semiconductors. *Physica* **1967**, *34*, 149–154. [CrossRef]

71. Vuong, N.M.; Kim, D.; Kim, H. Surface gas sensing kinetics of a WO_3 nanowire sensor: Part 1-Oxidizing gases. *Sensors Actuators B Chem.* **2015**, *220*, 932–941. [CrossRef]